JGR Space Physics

RESEARCH ARTICLE
10.1029/2022JA030716

**Key Points:**

- Mesoscale high-latitude electric fields significantly impact the thermospheric energy budget via enhanced Joule heating
- A 1 mW/m$^2$ enhancement in the total power flux can induce 50 K neutral temperature increase above 200 km altitude
- The excess energy deposits within a few minutes to increase the neutral density above 250 km altitude and accelerate the neutral wind

**Correspondence to:**
X. Meng,
xing.meng@jpl.nasa.gov

**Citation:**
Meng, X., Ozturk, D. S., Verkhoglyadova, O. P., Varney, R. H., Reimer, A. S., Semeter, J. L., et al. (2022). Energy deposition by mesoscale high-latitude electric fields into the thermosphere during the 26 October 2019 geomagnetic storm. *Journal of Geophysical Research: Space Physics*, *127*, e2022JA030716. https://doi.org/10.1029/2022JA030716

Received 2 JUN 2022
Accepted 12 DEC 2022



# Energy Deposition by Mesoscale High-Latitude Electric Fields Into the Thermosphere During the 26 October 2019 Geomagnetic Storm

**Xing Meng[1], Dogacan S. Ozturk[2], Olga P. Verkhoglyadova[1], Roger H. Varney[3,4], Ashton S. Reimer[3], Joshua L. Semeter[5], Stephen R. Kaeppler[6], and Weijia Zhan[6,7]**

[1]Jet Propulsion Laboratory, California Institute of Technology, Pasadena, CA, USA, [2]University of Alaska Fairbanks, Fairbanks, AK, USA, [3]SRI International Menlo Park, Menlo Park, CA, USA, [4]Now at Department of Atmospheric and Oceanic Sciences, University of California, Los Angeles, CA, USA, [5]Center for Space Physics and Department of Electrical and Computer Engineering, Boston University, Boston, MA, USA, [6]Clemson University, Clemson, SC, USA, [7]Now at Space Weather Technology, Research and Education Center (SWx TREC), University of Colorado Boulder, Boulder, CO, USA

**Abstract** Mesoscale high-latitude electric fields are known to deposit energy into the ionospheric and thermospheric system, yet the energy deposition process is not fully understood. We conduct a case study to quantify the energy deposition from mesoscale high-latitude electric fields to the thermosphere. For the investigation, we obtain the high-latitude electric field with mesoscale variabilities from Poker Flat Incoherent Scatter Radar measurements during a moderate geomagnetic storm, providing the driver for the Global Ionosphere and Thermosphere Model (GITM) via the High-latitude Input for Mesoscale Electrodynamics framework. The HIME-GITM simulation is compared with GITM simulations driven by the large-scale electric field from the Weimer model. Our modeling results indicate that the mesoscale electric field modifies the thermospheric energy budget primarily through enhancing the Joule heating. Specifically, in the local high-latitude region of interest, the mesoscale electric field enhances the Joule heating by up to five times. The resulting neutral temperature enhancement can reach up to 50 K above 200 km altitude. Significant increase in the neutral density above 250 km altitude and in the neutral wind speed are found in the local region as well, lagging a few minutes after the Joule heating enhancement. We demonstrate that the energy deposited by the mesoscale electric field transfers primarily to the gravitational potential energy in the thermosphere.

**Plain Language Summary** The high-latitude region of the terrestrial upper atmosphere is an important pathway of solar wind energy deposition into the atmosphere. The electric field in the high-latitude region varies temporarily and spatially on a variety of scales. This modeling study investigates the impact of mesoscale electric field variability, where mesoscale is defined as a spatial scale between 100 and 500 km and a temporal scale between 2 and 15 min. We utilize numerical modeling and ground-based radar observations to quantify the impact of mesoscale electric fields on the heating and dynamics of the high-latitude upper atmosphere during a geomagnetic storm. Our results indicate that mesoscale electric fields induce significant enhancement in the Joule heating, temperature, density, and wind of the upper atmosphere.

## 1. Introduction

The high-latitude electric field is a crucial driver of the ionospheric and thermospheric system and provides a primary energy source for the thermosphere in the form of Joule heating (Kaeppler et al., 2022; G. Lu et al., 2016). The high-latitude electric field changes spatially and temporally on a variety of scales (Codrescu et al., 2000; Cousins & Shepherd, 2012; Crowley & Hackert, 2001; Matsuo et al., 2003). Such variability of the electric field, especially the small-scale and mesoscale variability that has long been absent in empirical models of the high-latitude electric field, can significantly impact the thermospheric Joule heating, neutral density, and neutral temperature (Codrescu & Fuller-Rowell, 1995; Codrescu et al., 2008; Deng et al., 2008, 2009; Golovchanskaya, 2008; Matsuo & Richmond, 2008; Wu et al., 2020; Q. Zhu et al., 2018, 2019). In particular, small-scale and mesoscale electric field variabilities could contribute even more to the Joule heating than the large-scale averaged electric field does (Deng et al., 2009; Matsuo & Richmond, 2008). Here we refer mesocale as a spatiotemporal scale between small-scale and large-scale, with a spatial scale between 100 and 500 km and a temporal scale between 2 and 15 min (Ozturk et al., 2020).

Recognizing the importance of the small-scale and mesoscale electric field variabilities, their quantitative influence on the thermospheric dynamics has been investigated in a number of efforts. These efforts are primarily modeling studies that adapt small-scale and/or mesoscale electric fields, in addition to the large-scale electric field, to drive general circulation models (GCMs) of the global ionosphere and thermosphere. GCMs that have been used in these modeling studies include: Coupled Thermosphere Ionosphere Plasmasphere Electrodynamics (CTIPE) (Millward et al., 1996, 2001), Thermosphere Ionosphere Electrodynamics General Circulation Model (TIEGCM) (Richmond et al., 1992), and Global Ionosphere and Thermosphere Model (GITM) (Ridley et al., 2006). Specifically, Codrescu et al. (2008) imposes small-scale fluctuations to the large-scale electric field provided by empirical model Weimer (2005), which is used to drive CTIPE. The modeling result indicates that the thermospheric temperature at 300 km altitude is higher and better reproduced if including the small-scale electric field variability compared to excluding it. Matsuo and Richmond (2008) incorporates the small-scale and mesoscale electric field variability derived from Dynamic Explorer-2 (DE-2) measurements into driving the TIEGCM. They show that small-scale and mesoscale electric fields modify the global Joule heating rate and neutral wind in the thermosphere. Deng et al. (2009) develop the first self-consistent empirical model with electric field variabilities of all scales derived from DE-2 observations. TIEGCM simulations driven by empirical models with and without the electric field variability reveal that the electric field variability induces a more than 100% increase in the hemispherically-integrated Joule heating, a 120 K increase in the polar average temperature at 400 km altitude, and a nearly 30% increase in the polar average neutral density at 400 km altitude. Q. Zhu et al. (2018) conducts GITM simulations driven by the average electric field and its large-scale variability versus including the small-scale and mesoscale variability, which are obtained from the statistical analysis of DE-2 observations. They find a 27% increase in the hemispherically-integrated Joule heating in the simulation including the small-scale and mesoscale variability, compared to the simulation without it. Wu et al. (2020) show that including the small-scale and mesoscale variability in the electric field and particle precipitation allows the TIEGCM to reproduce observed characteristics of storm-time thermospheric temperature enhancement and inversion layer in the Antarctic E region. X. Lu et al. (2021) assimilate ground-based and space-borne data to provide multi-scale two-dimensional electric field and particle precipitation patterns for the TIEGCM simulation of an intense geomagnetic storm. They discover strong vertical neutral winds when both the electric field and the particle precipitation are enhanced. Moreover, they find that the assimilation of Poker Flat Incoherent Scatter Radar (PFISR) derived electric field data is critical to reproduce observed neutral quantities locally. All these research efforts have undoubtedly advanced the understanding of the thermospheric response to small-scale and mesoscale electric fields. However, our knowledge is still incomplete regarding the detailed physical process of the energy deposition from small-scale and mesoscale electric fields into the thermosphere.

In this work, we quantify the impact of the mesoscale electric field on the thermospheric energy budget and the resulting neutral dynamics during a moderate geomagnetic storm using numerical modeling. The objectives of the work are (a) to describe and understand the thermospheric energy partition and deposition under mesoscale electric field driving, and (b) to validate and demonstrate the applicability of incorporating mesoscale variabilities in the high-latitude electric field for ionospheric and thermospheric modeling. We take advantage of the recently developed High-latitude Input for Mesoscale Electrodynamics (HIME) framework (Ozturk et al., 2020) and its interface with GITM. HIME maps the electric field derived from PFISR measurements, which naturally contains mesoscale variabilities, to the high-latitude grid of GITM, thus providing the mesoscale electric field driving for GITM. Note that HIME can also work with GCMs other than GITM, but the software interface between HIME and other GCMs has not been developed. Therefore, for the present work we utilize the fully developed HIME-GITM interface. We compare the HIME-driven GITM simulation with the GITM simulation driven by empirical large-scale electric field model Weimer to investigate how the mesoscale electric field modifies thermospheric heating and cooling in the local region of PFISR. The simulated height-integrated Joule heating is validated against the Joule heating derived from PFISR measurements. Moreover, we examine the neutral responses to a localized outstanding Joule heating enhancement and the heating-induced temporal and vertical variations in the neutral density and neutral wind. As a result, we gain insight into the pathways of the energy deposition in the thermosphere. Unlike most previous research efforts that investigate the global impact of the mesoscale electric field and height-integrated responses of the thermosphere, our work highlights the impact of the mesoscale electric field in a localized region and at various altitudes for the first time. Although we recognize the correlation between small-scale and mesoscale high-latitude electric field and particle precipitation in the resulting thermospheric Joule heating (Baker et al., 2004; Evans et al., 1977; Sheng et al., 2019; Q. Zhu

et al., 2018), we focus on the impact of the mesoscale electric field and exclude the mesoscale particle precipitation in the work.

The following content of the paper is divided into three parts. Section 2 reviews HIME-GITM and presents the modeling setup for the specific geomagnetic storm. Section 3 reports the modeling results, including the data-model comparison of Joule heating and the thermosphere energy and neutral response to the inclusion of the mesoscale electric field. Section 4 concludes the paper.

## 2. Methodology

Utilizing PFISR measurements, we carry out GITM simulations and analyze the simulation results for an extended time period during the 26 October 2019 geomagnetic storm. We also compare the simulated Joule heating with the observationally-derived Joule heating data. Below we describe the observational data and our modeling setup in detail.

### 2.1. Observational Data

For this work, a specifically designed PFISR experiment "GITM1. v01" (https://data.amisr.com/database/61/experiment/20191026.002/1/) was conducted during 26–30 October 2019, which covers the recovery phase of a moderate geomagnetic storm with the minimum Dst of −46 nT. The experiment consisted of 22 Long Pulse beams and 11 Alternating Code beams. From the line-of-sight plasma velocity measurements made by the Long Pulse beams, we obtain the F region electric field on a 2D grid that covers a 7.5° latitudinal and 16.5° longitudinal region surrounding PFISR (Nicolls et al., 2014). The grid size is about 0.15° in magnetic latitude and 0.34° in magnetic longitude. The temporal resolution of the electric field is 66 s. Owing to the fine spatial and temporal resolutions, the PFISR-estimated electric field includes not only the large-scale variability but also the mesoscale variability.

Joule heating can be derived from PFISR measurements following the algorithm described in Zhan et al. (2021), in order to validate the simulated Joule heating. It is important to note that the Joule heating data is processed in a different way than the PFISR-derived electric fields used in the HIME, even though both data products are derived from the same source data, that is, PFISR experiment GITM1.v01. For the Joule heating data, the electric field is estimated using the algorithm described by (Heinselman & Nicolls, 2008). For this analysis, we use all of the F-region line-of-sight look directions to produce a single estimate of the electric field vector over the whole F-region volume. By using this method we are inherently assuming the plasma drifts in the F-region are spatially uniform over the F-region volume. The Alternating Code data are used to estimate the Pedersen conductivity, using formulas described in Zhan et al. (2021). We only consider the vertically pointed beam PFISR beam for the estimation of the Pedersen conductivity spanning from 90 to 250 km with a 5 km altitude increment. We altitudinally integrate the Pedersen conductivity and merge the Pedersen conductance with the single electric field vector to produce the passive energy deposition rate, that is, the passive Joule heating, in this context. We therefore interpret the PFISR-derived passive Joule heating data as corresponding to a spatially average passive energy deposition rate.

### 2.2. Modeling Approach

HIME is a framework to incorporate local mesoscale high-latitude drivers into the forcing of global GCMs of the upper atmosphere (Ozturk et al., 2020). The existing open-source HIME version 1.0 focuses on incorporating the mesoscale electric field, while the capability of including the mesoscale auroral particle precipitation is under development and will be reported in a future publication. Ozturk et al. (2020) presents the first application of HIME that uses PFISR-estimated 2D electric field as an upper boundary condition to drive GITM. The estimated electric field in the local region is merged with the global large-scale electric field from the Weimer model using a Gaussian filter for a smooth transition. The combined electric field is then provided to GITM as the high-latitude electric field driver. An optimal horizontal grid resolution for HIME-driven GITM simulation is found to be 0.75°, which is capable of resolving mesoscale structures in the estimated electric field from PFISR measurements meanwhile being computationally effective. The modeling results indicate the successful integration of the observationally estimated mesoscale electric field to GITM. The inclusion of the mesoscale electric field

**Table 1**
*High-Latitude Driver Settings for Global Ionosphere and Thermosphere Model Runs*

| Run | High-latitude electric field | High-latitude precipitation |
|---|---|---|
| Weimer-driven run 1 | Weimer | OVATION Prime |
| Weimer-driven run 2 | Weimer with enhancement | OVATION Prime |
| HIME-driven run | PFISR estimates | OVATION Prime |

in the driving of GITM leads to increased energy deposition and elevated ion temperature in the PFISR local region during a weak geomagnetic storm.

Utilizing the existing HIME version 1.0 and its interface with GITM, we perform HIME-driven GITM modeling for a selected time interval of five hours, from 7UT to 12UT on 26 October 2019. During the selected time interval, the AE index varies between 500 and 20,00 nT, indicating moderate substorm activities. In addition to the HIME-driven GITM simulation, we also perform a Weimer-driven GITM simulation to provide a baseline for comparison. The specific modeling setup is as following: First, we run a 2-day warm-up GITM simulation covering from 0UT on 24 October 2019 to 6UT on 26 October 2019. The horizontal grid resolution is 0.75° in both longitude and latitude, and the vertical grid size is one third of the local scale height. In the warm-up simulation, the high-latitude electric field is provided by the Weimer model and the high-latitude particle precipitation is specified by the empirical model OVATION Prime (Newell et al., 2009). The initial condition and the lower boundary conditions are specified by Mass Spectrometer and Incoherent Scatter model (Hedin, 1991) and Horizontal Wind Model (Drob et al., 2008). The input of the simulation includes the 1-min resolution OMNI solar wind data (Papitashvili & King, 2020), for driving the Weimer and OVATION Prime models, and the solar extreme ultraviolet (EUV) spectra from the Flare Irradiance Spectral Model (FISM) (Chamberlin et al., 2008). Second, we conduct three six-hour GITM simulations restarted from the solutions of the warm-up GITM simulation, to cover the time period between 6UT and 12UT on 26 October 2019. All three simulations use the same grid resolution and the same ways of specifying the high-latitude particle precipitation, lower boundary condition, and the solar EUV irradiance as the warm-up simulation. The only difference among the three simulations is the high-latitude electric field. In Weimer-driven run 1, the high-latitude electric field is still provided by the Weimer model. In Weimer-driven run 2, the high-latitude electric field is taken from the Weimer model, with a constant enhancement (15.966 mV/m) added to the electric field magnitude while keeping the electric field direction unchanged within the local region of PFISR. This electric field enhancement is obtained by subtracting the average of the Weimer electric field magnitude from the average of the PFISR electric field magnitude, where "average" is the spatial and temporal average over the PFISR local region during 7UT–12UT. As a result, the enhancement brings the spatial and temporal average of the Weimer electric field magnitude up to the same value as the spatial and temporal average of the PFISR electric field amplitude in the local region. In the HIME-driven run, the high-latitude electric field is specified by the PFISR estimates in the local region of PFISR and by the Weimer model elsewhere. The high-latitude driving conditions for the three runs are summarized in Table 1. We allow the electric field to take its full effect during the first hour of the HIME-driven GITM run, from 6UT to 7UT, which is considered a warm-up time for the mesoscale electric field input. We focus our analysis of the modeling result on the selected five-hour time interval between 7UT and 12UT.

The simulated horizontal electric field in the local region surrounding PFISR is displayed in Figure 1. In Weimer-driven GITM run 1, the electric field at the displayed high-latitude region is solely from the Weimer model. In the HIME-driven GITM run, the horizontal electric field is dominated by the electric field estimates from PFISR measurements in the region covered by the Long Pulse beams and by the electric field from the Weimer model outside the Long Pulse beam region. As expected, a much more enhanced and structured horizontal electric field is found within the Long Pulse beam region comparing to the region outside. This is distinctive at 10:16 UT from the HIME-driven run shown in Figure 1b. Such enhancement and fine structures are absent in the electric field from the Weimer-driven run 1 shown in Figure 1b. The time series of the PFISR-estimated and GITM-simulated horizontal electric field magnitude averaged within 152°–142°W and 65.5°–69.5°N, the central region covered by PFISR Long Pulse beams, are displayed in Figure 1c. The magnitude and temporal variations of the PFISR-estimated electric field are mostly conveyed into the HIME-driven run. Overall, the electric field is up to five times more intense in the HIME-driven run than in Weimer-driven run 1. This motivates the set up of Weimer-driven run 2, which has an elevated horizontal electric field magnitude compared to Weimer-driven run 1, while the electric field direction, spatial and temporal variabilities are the same as those in Weimer-driven run 1. Comparing the HIME-driven run to Weimer-driven run 2, the spatially-averaged horizontal electric field from the HIME-driven run exhibits more temporal variations, especially on temporal scales of minutes according to Figure 1c. In particular, the magnitude of the electric field from the HIME-driven run has a temporal variability comparable to the magnitude of the electric field itself (on the order of tens of mV/m), which is consistent with

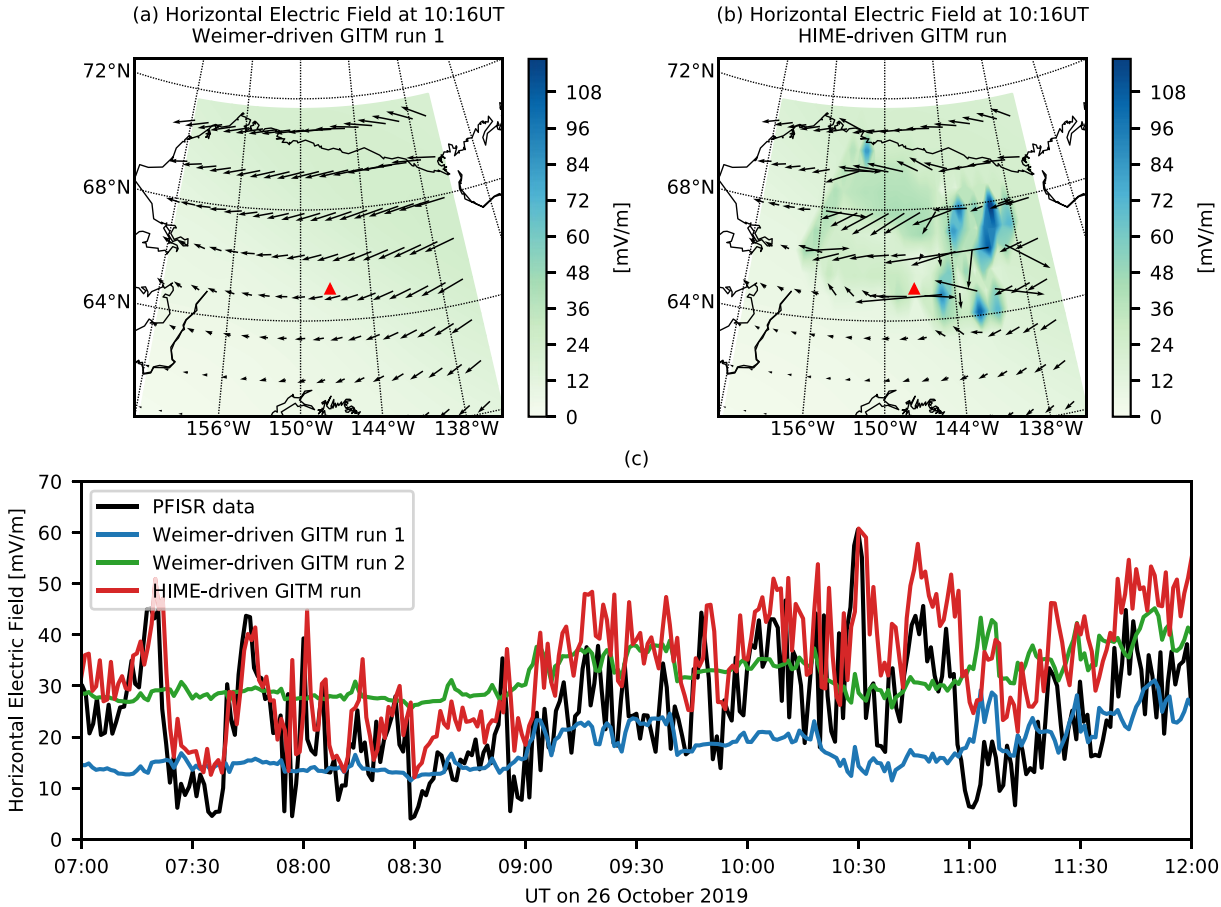


**Figure 1.** The simulated horizontal electric field at 10:16UT from Weimer-driven Global Ionosphere and Thermosphere Model (GITM) run 1 (panel (a)) and the HIME-driven GITM run (panel (b)) at 250 km altitude. The arrows indicate the horizontal electric field vectors, while the color contour represents the magnitude of the horizontal electric field. The red triangle marks the location of Poker Flat Incoherent Scatter Radar. (c) The horizontal electric field magnitude averaged within 152°–142°W and 65.5°–69.5°N at 250 km altitude.

the statistical observational finding that the electric field variability can be as large as the mean climatological electric field (Matsuo et al., 2003). The mesoscale variabilities of the electric field significantly alter the local thermospheric energy budget and neutral dynamics, as reported in the next Section.

## 3. Results

In the Section, we limit our analysis of the modeling result to the central region of the PFISR Long Pulse beam coverage, that is, within 152°–142°W and 65.5°–69.5°N. This is to avoid any impact of the Weimer-model-provided electric field near the boundaries of the Long Pulse beam region. Within the selected local region, the horizontal electric field is specified by the electric field estimates from PFISR measurements and exhibits mesoscale spatial and temporal variabilities. The local thermospheric responses to the mesoscale electric field are investigated.

### 3.1. Joule Heating

The Joule heating can be broken down into the passive Joule heating and the mechanical energy transfer contributed by the neutral wind (Kaeppler et al., 2022). Given the observationally-derived passive Joule heating, we calculate the simulated passive Joule heating to compare with the observation. The simulated passive Joule heating is calculated by extracting the Pedersen conductivity and electric field from the GITM simulations, multiplying the Pedersen conductivity with the square of the electric field magnitude, and then spatially averaging within the PFISR local region. The comparison between the simulated and observationally-derived height-integrated passive

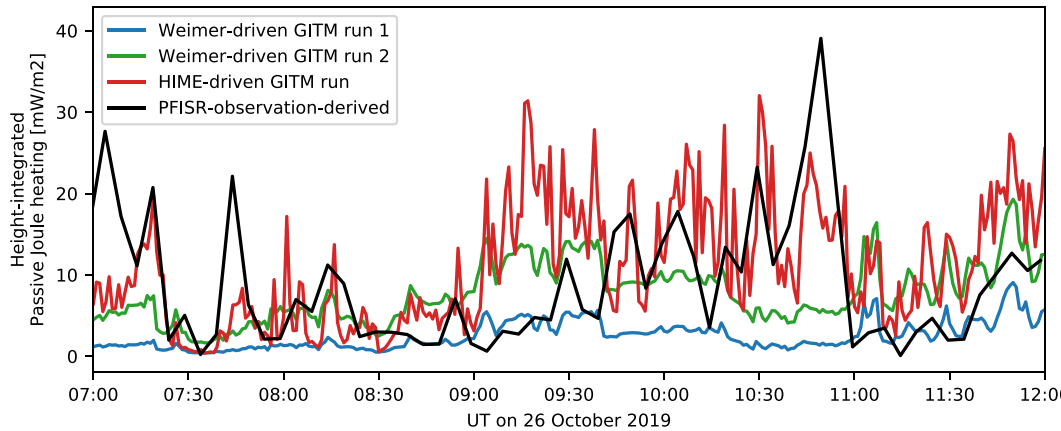


**Figure 2.** Comparison between simulated and observationally-derived height-integrated passive Joule heating averaged within 152°–142°W and 65.5°–69.5°N. Please see Section 2.1 for more details regarding the calculation of the observationally-derived passive Joule heating.

Joule heating is displayed in Figure 2. Specifically, the height integral is taken for the altitudes between 100 and 250 km in the simulations. The specific altitude range is chosen to match the overlap altitude range between GITM simulations and the observationally-derived passive Joule heating data. This altitude range should cover the peak of passive Joule heating along the vertical direction. We point out that both simulated and observationally-derived passive Joule heating are the heating power density in unit of $W/m^3$. The height-integrated passive Joule heating is essentially the heating power flux in unit of $W/m^2$. Note that the simulated passive Joule heating has a temporal resolution of 1 min, while the observationally-derived passive Joule heating has a temporal resolution of 5 min. Based on Figure 2, the HIME-driven run generates largest passive Joule heating with most temporal variabilities among the three runs, which matches with the observationally-derived passive Joule heating much better than the Weimer-driven runs. The fairly good agreement between the passive Joule heating from the HIME-driven run and the observation also validates the HIME-driven GITM modeling result for the five-hour time interval of interest. Weimer-driven run 2 generates higher passive Joule heating than Weimer-driven run 1, due to the enhancement of the electric field in Weimer-driven run 2. However, during the majority of the time interval, Weimer-driven run 2 produces lower passive Joule heating than the HIME-driven run, even though the temporal and regional average electric fields from the two runs are the same. This indicates that the mesoscale electric field variability enhances the passive Joule heating. To investigate and quantify the impact of the mesoscale electric field variability, the rest of Section 3 focuses on Weimer-driven run 2 and the HIME-driven run only.

To examine the impact of the mesoscale electric field variability on the Joule heating at various altitudes, we display the simulated Joule heating as a function of time and altitude in Figure 3. The simulated Joule heating is equivalent to the total Joule heating consisted of the passive Joule heating and the mechanical energy transfer below 400 km altitude (Kaeppler et al., 2022). Moreover, the displayed Joule heating values are averages within 152°–142°W and 65.5°–69.5°N. Comparing the HIME-driven run to Weimer-driven run 2, multiple short-lived Joule heating enhancements occur during 7UT and 12UT and are peaked around 120 km altitude, visible in the middle panel of Figure 3. These enhancements can reach as large as five times of the Joule heating values from Weimer-driven run 2, indicating the dominant role of the mesoscale electric field driving in generating the Joule heating for the lower thermosphere.

### 3.2. Energy Budget

The thermospheric energy budget is contributed from a number of energy sources and sinks (Verkhoglyadova et al., 2016, 2017). With GITM, one can separately investigate the individual energy sources and sinks, represented by the heating and cooling terms in the neutral temperature equation (Ridley et al., 2006). These heating and cooling terms include: EUV heating, photoelectron heating, Joule heating, auroral heating, chemical heating, conduction, O cooling, NO cooling, and $CO_2$ cooling. Same as the Joule heating, other heating and cooling terms from GITM are power densities in unit of $W/m^3$. In the local region of interest, 152°–142°W and 65.5°–69.5°N, the EUV heating and photoelectron heating are absent from 7UT to 12UT, as it is during the local night time.

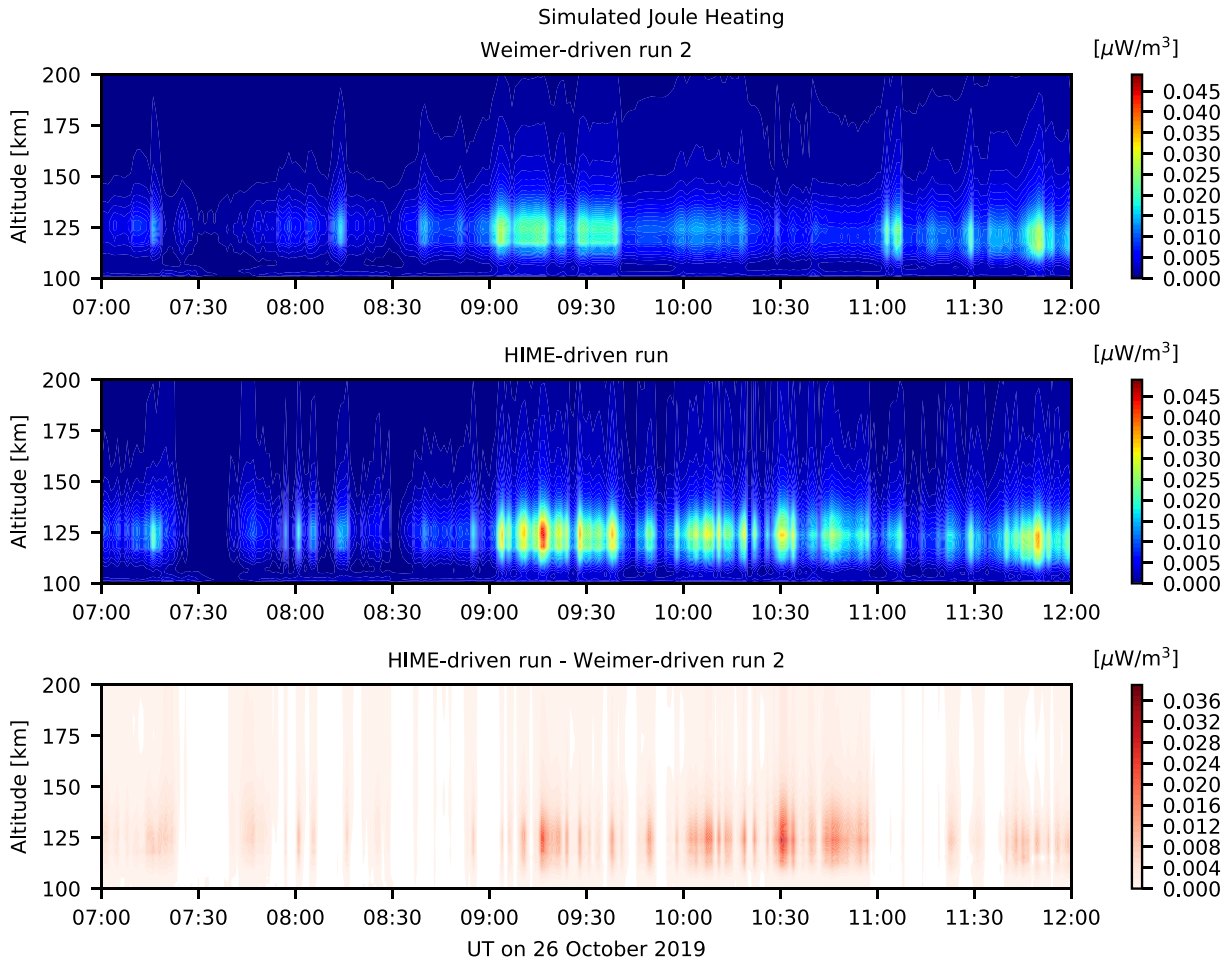


**Figure 3.** Simulated Joule heating averaged within 152°–142°W and 65.5°–69.5°N and displayed as a function of time and altitude from Weimer-driven Global Ionosphere and Thermosphere Model (GITM) run 2 (top panel) and the HIME-driven GITM run (middle panel). The difference between the Joule heating from the HIME-driven run and from the Weimer-driven run is shown in the bottom panel.

For each of the remaining heating and cooling terms, we calculate the height-integrated value and take the average within 152°–142°W and 65.5°–69.5°N for both the Weimer-driven and HIME-driven GITM runs. Note that the height integrals are taken for all altitudes covered by the GITM runs for this event, which are between 100 and 500 km. The results are displayed in Figure 4. Among all heating terms and for both Weimer-driven and HIME-driven runs, the dominate heating terms are the Joule heating and auroral heating that represents the heating introduced by auroral particle precipitation. Among all cooling terms, the $CO_2$ cooling is the largest at all time and for both Weimer-driven and HIME-driven runs. The mesoscale electric field driving impacts the Joule heating most comparing to the rest of the heating and cooling terms, causing various amount of increase and fluctuations in Joule heating at different time. The mesoscale electric field driving also enhances the NO cooling term noticeably. Unlike the Joule heating and NO cooling, changes in the other heating and cooling terms due to the mesoscale electric field driving are tiny portions of their background values.

Considering all heating and cooling terms shown in Figure 4, we calculate the total heating, total cooling, and total power flux for every minute during 7UT and 12UT, displayed in Figure 5a. At a given time, the total heating, or more precisely, the total heating power flux, is obtained by adding up all height-integrated heating terms, and the total cooling, or total cooling power flux, is obtained by adding up all height-integrated cooling terms (negative values). The total heating plus the total cooling yields the total power flux in unit of $W/m^2$. A positive total power flux indicates net heating, and a negative total power flux indicates net cooling. While the total cooling remains nearly identical in the Weimer-driven and HIME-driven runs, the total heating is larger and shows more temporal variations in the HIME-driven run than in Weimer-driven run 2, especially during 9UT–11UT.

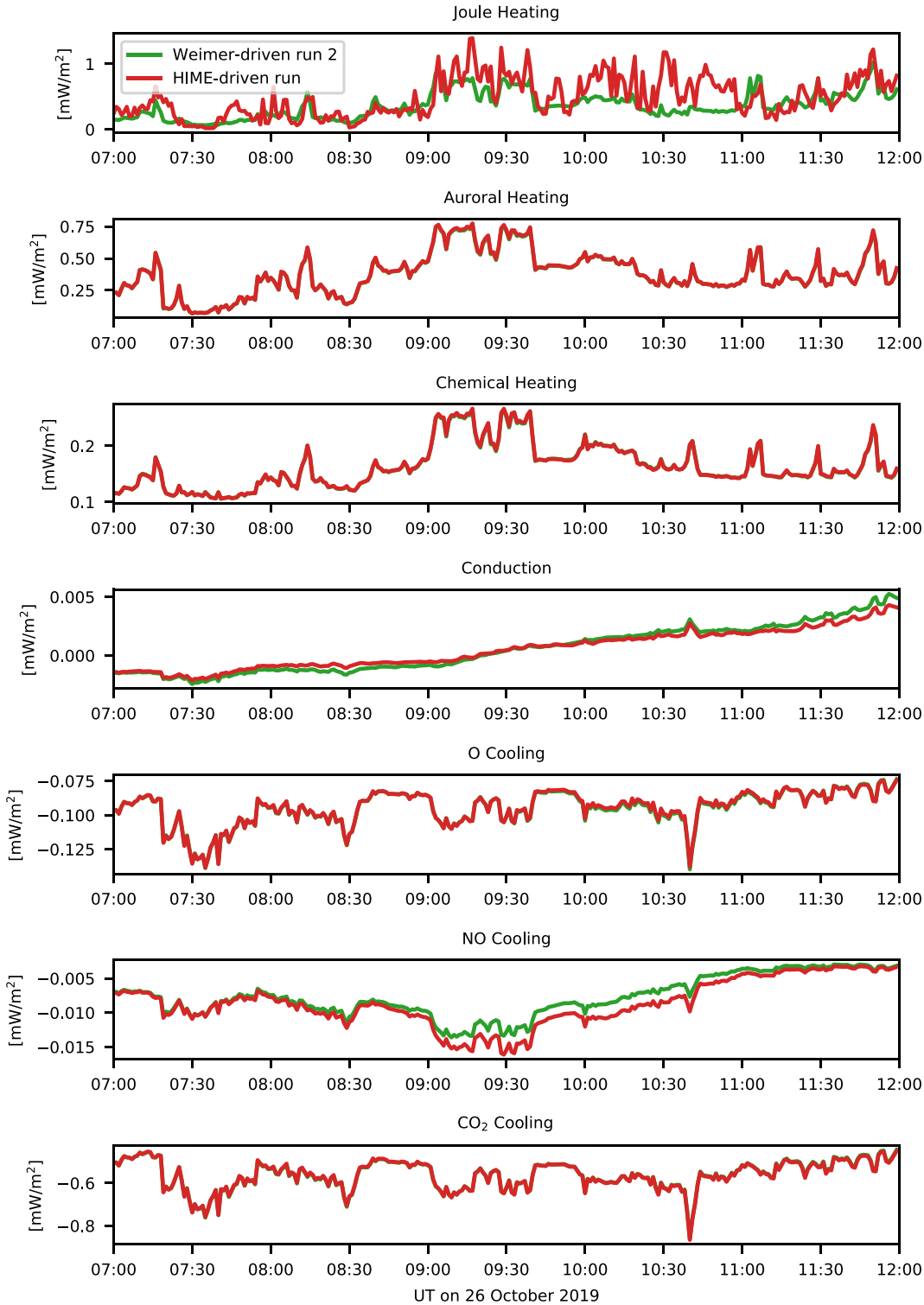


**Figure 4.** Simulated height-integrated heating and cooling averaged within 152°–142°W and 65.5°–69.5°N as a function of time.

The enhancement in the total heating is primarily caused by the enhancement in the Joule heating induced by the mesoscale electric field driving. The total power flux inherits the enhancement and temporal variations from the total heating, leading to higher net heating during most of the time in the HIME-driven run than in Weimer-driven run 2. Figure 5b presents the difference between the total power flux the HIME-driven run and total power flux

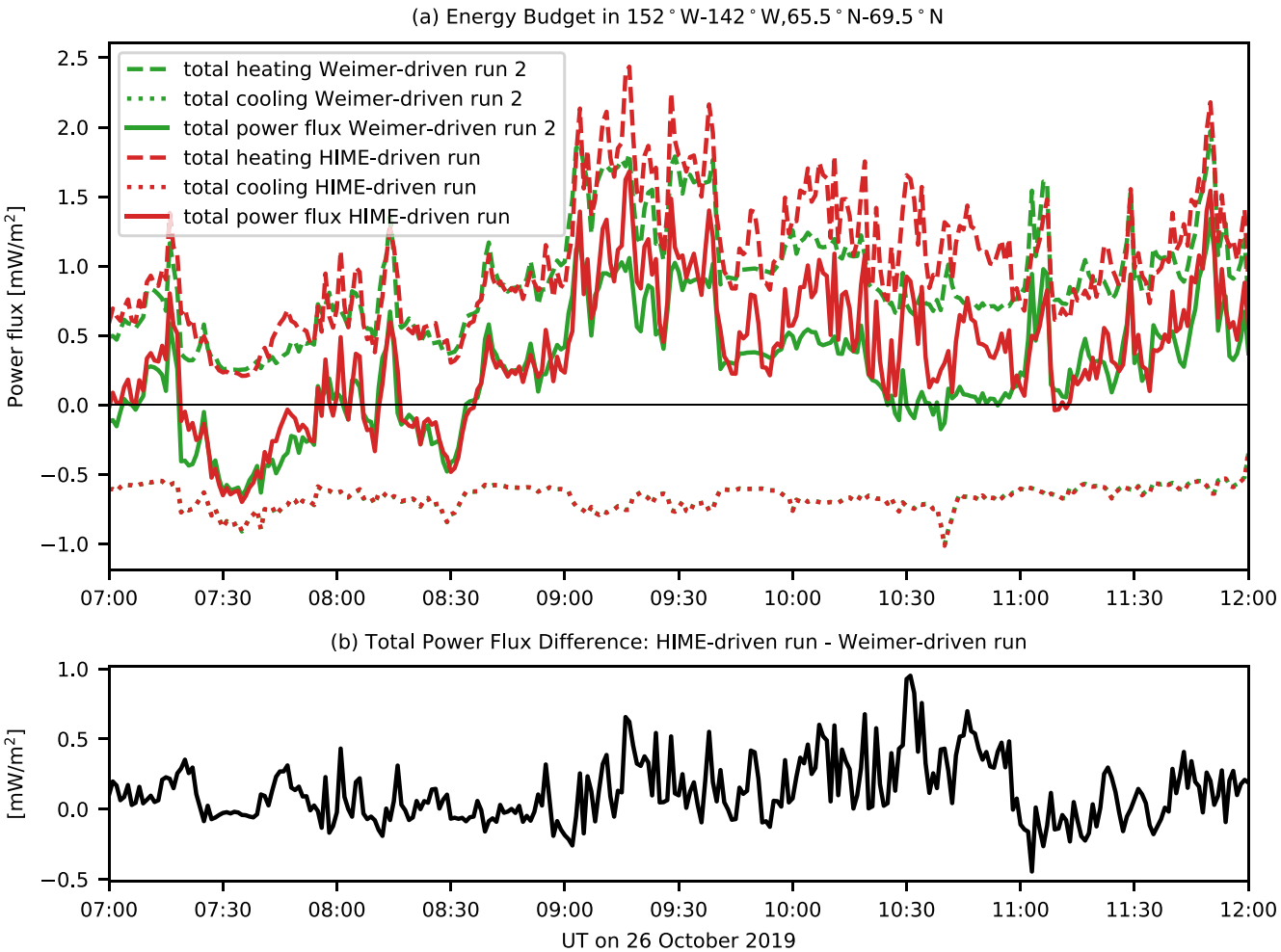


**Figure 5.** (a) Simulated total heating, total cooling, and total power flux averaged within 152°–142°W and 65.5°–69.5°N. (b) The difference between the total power flux from the HIME-driven Global Ionosphere and Thermosphere Model (GITM) run (red solid line in (a)) and the total power flux from Weimer-driven GITM run 2 (green solid line in (a)).

from Weimer-driven run 2. The total power flux difference varies between −0.5 and 1.0 mW/m$^2$ with time, and the largest difference occurs around 10:30UT. The value of the total power flux difference is comparable to the absolute value of the total power flux itself from Weimer-driven run 2, implying the prevailing role of the mesoscale electric field driving in shaping the thermospheric energy balance at high-latitudes.

### 3.3. Neutral Temperature and Density

The total power flux shown in Figure 5 serves as the source term for the neutral temperature equation in GITM thus is directly related to the simulated neutral temperature. Displayed in Figure 6, the neutral temperature from the Weimer-driven and the neutral temperature from the HIME-driven runs are distinctively different. The neutral temperature from the HIME-driven run shows stronger temporal variations and reaches higher values at time of enhancement compared to the neutral temperature from Weimer-driven run 2. According to the neutral temperature difference in the bottom panel of Figure 6, the neutral temperature enhancements caused by the mesoscale electric field driving can reach as large as 50 K around 10:30UT, which corresponds to about 1 mW/m$^2$ total power flux difference in Figure 5b. The temperature enhancements start at altitudes between 200 and 300 km, and they reach 500 km altitude within a few minutes or less. At altitudes above 300 km, the neutral temperature enhancements are almost always followed by the neutral temperature reduction. Referencing to Figure 5b, it is evident that the time of neutral temperature enhancements, that is, positive neutral temperature

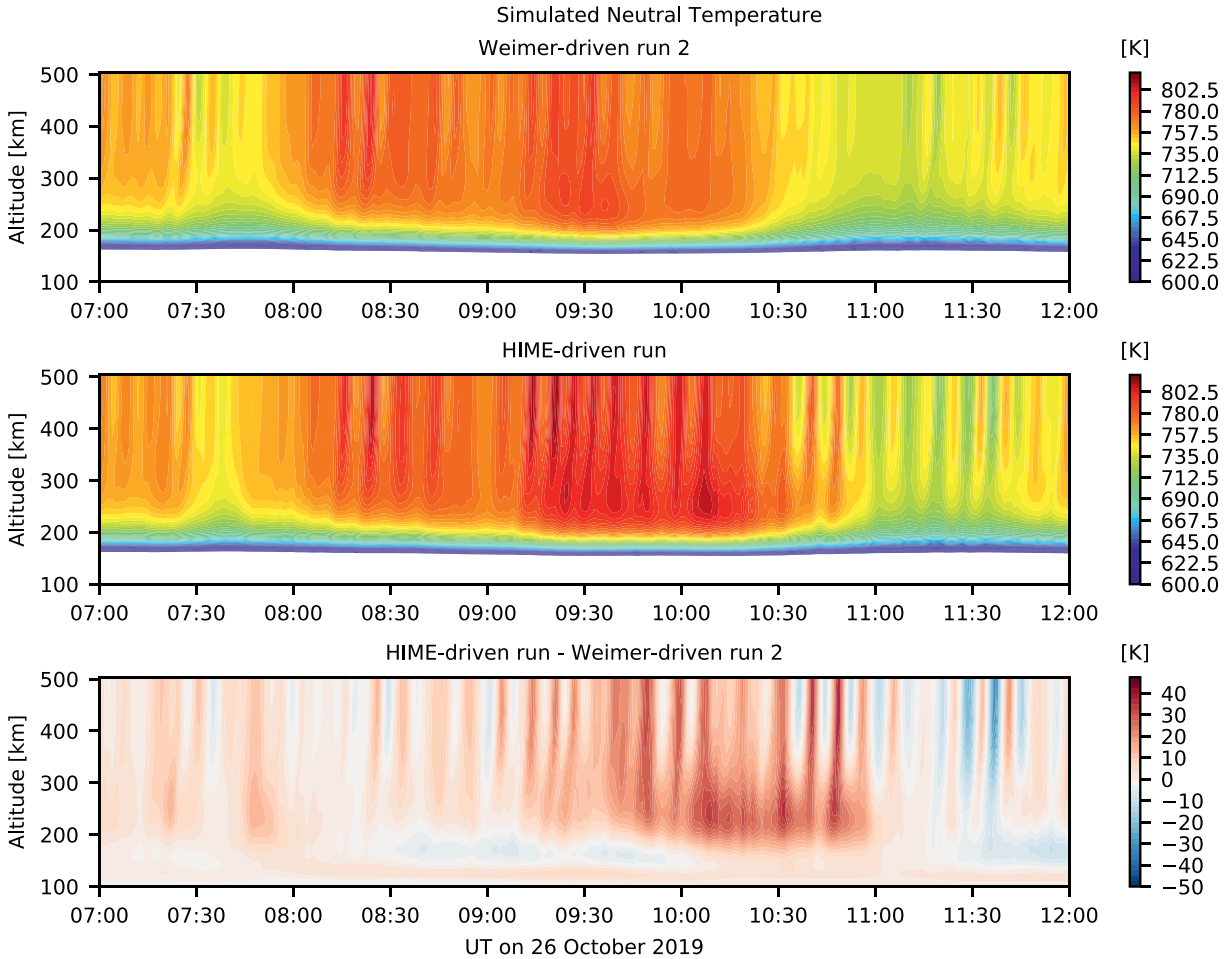


**Figure 6.** Simulated neutral temperature averaged within 152°–142°W and 65.5°–69.5°N and displayed as a function of time and altitude from Weimer-driven Global Ionosphere and Thermosphere Model (GITM) run 2 (top panel) and the HIME-driven GITM run (middle panel). The difference between the neutral temperature from the HIME-driven run and from Weimer-driven run 2 is shown in the bottom panel.

differences, correspond to the time of the peaks in the total power flux difference. Moreover, the large neutral temperature difference between 9UT and 11UT is consistent with the large total power flux difference during the same time interval.

To evaluate the response of the thermospheric density to the mesoscale electric field driving, we visualize the simulated neutral density in Figure 7. Examining the neutral density from the Weimer-driven and HIME-driven runs, the latter produces more prominent wave-like structures in the neutral density, which is especially visible above 400 km altitude. These wave-like structures are caused by the periodic enhancement of total power flux and neutral temperature. From the percentage difference of the neutral density shown in the bottom panel of Figure 7, large differences between the neutral density from the Weimer-driven and HIME-driven runs are found at altitudes above 300 km. In particular, the neutral density from the HIME-driven run can be up to 40% larger than the neutral density from Weimer-driven run 2. The enhancements in the neutral density due to the mesoscale electric field driving start at around 300 km altitude and reach 500 km altitude within a few minutes. Similar to the neutral temperature, the neutral density enhancements are followed by neutral density reduction, indicating the restoration of the thermospheric gravitational potential energy. In addition, the largest enhancement of the neutral density occurs shortly after 10:30UT, which corresponds to the time of the largest total power flux difference shown in Figure 5b.

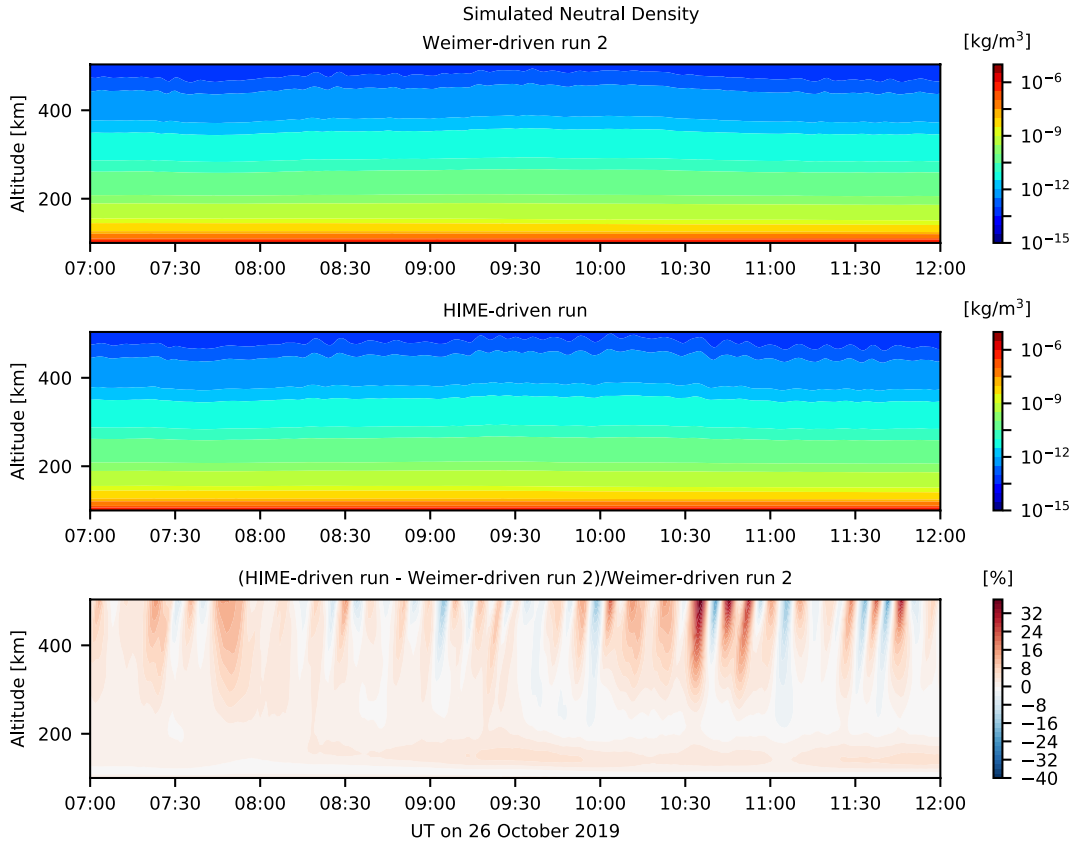


**Figure 7.** Simulated neutral density averaged within 152°–142°W and 65.5°–69.5°N and displayed as a function of time and altitude from Weimer-driven Global Ionosphere and Thermosphere Model (GITM) run 2 (top panel) and the HIME-driven GITM run (middle panel). The percentage difference between the neutral density from the HIME-driven run and from Weimer-driven run 2 is shown in the bottom panel.

### 3.4. Energy Deposition Pathways

According to the sign of the total power flux from Figure 5a, the HIME-driven run generates net heating during 9UT–12UT, indicating excess energy in the local region brought by the mesoscale electric field driving, as opposite to the approximately balanced energy during the same time interval from Weimer-driven run 2. To investigate pathways of the excess energy, we look into the detailed energy deposition process. Figure 8 displays vertical profiles of various quantities from 10:30UT to 10:35UT. Unlike the previous analysis that focuses on regional averaged quantities, the vertical profiles are taken at a specific grid point from the simulations, 144.375°W and 67.125°N. Analyzing quantities at a single grid point provides precise quantification of the impact from the mesoscale electric field driving at the grid cell level. The grid point and time interval are chosen at where and when a representative localized Joule heating enhancement due to the mesoscale electric field driving occurs. In particular, during the time interval, the maximum difference in the regional total power flux between the HIME-driven and Weimer-driven runs is found. Therefore, the analysis of this specific localized heating event would, to the largest extent, reveal the impact of the excess energy. In Figures 8a–8d and 8f–8i, the physical variable values from both the Weimer-driven and HIME-driven runs are displayed. Note that the vertical profiles from Weimer-driven run 2 vary little during 10:30UT–10:35UT, while the vertical profiles from the HIME-driven run exhibit much stronger temporal variations during the time interval. In Figure 8e, the neutral density difference is obtained by subtracting the solution of Weimer-driven run 2 from the solution of the HIME-driven run and normalizing to the solution of Weimer-driven run 2 at each corresponding time. This is to better visualize the temporal variation of the neutral density by removing the vertically decreasing neutral density background.

The total power density from the HIME-driven run shown in Figure 8a presents an enhancement at 10:31UT, with the peak value around 120 km altitude reaching at least five times of the peak value at 10:30UT. The enhancement weakens over time, and lasts for only 2 minutes. By 10:33UT, the total power density reduces

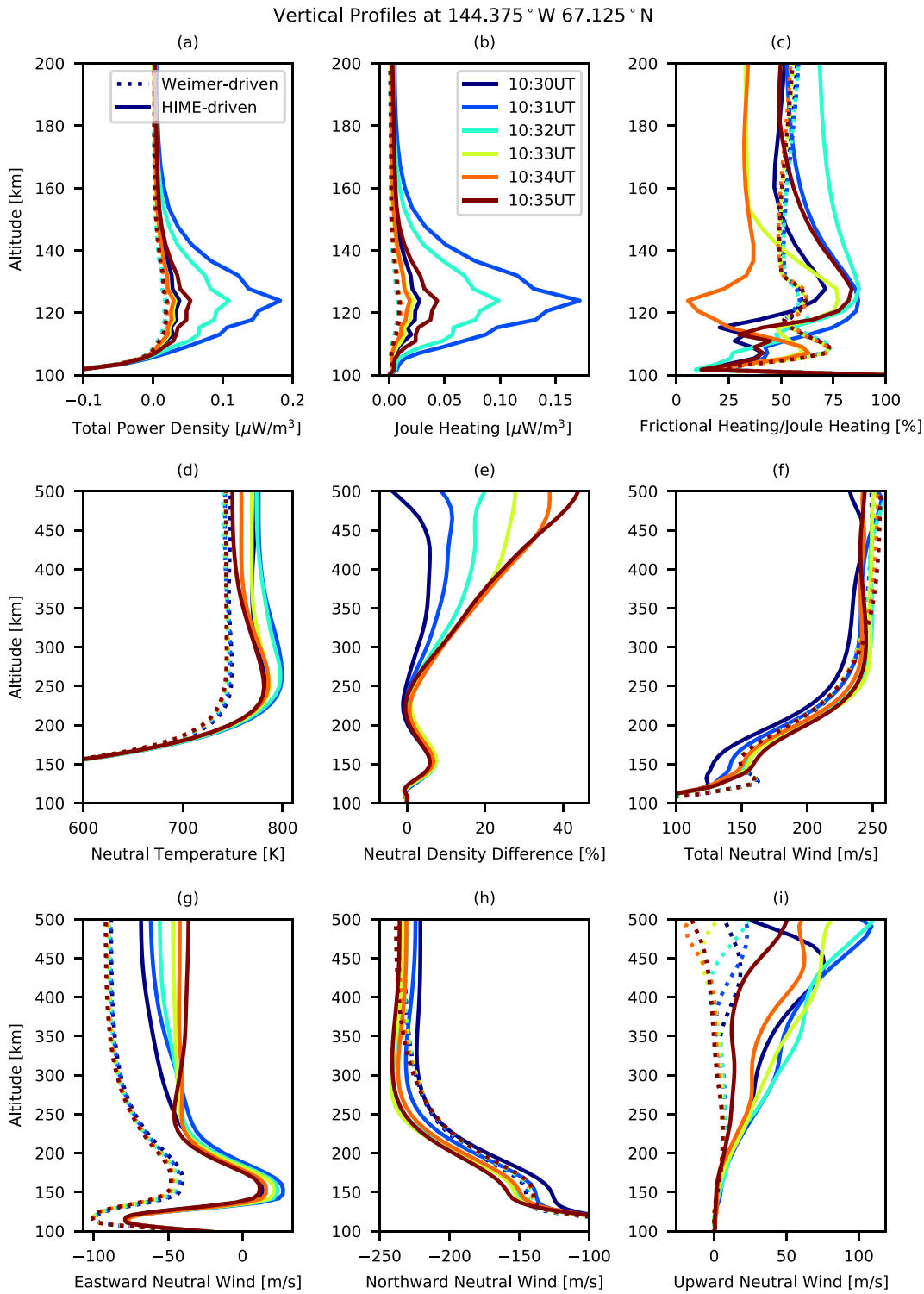


**Figure 8.** Simulated vertical profiles at 144.375°W and 67.125°N every minute from 10:30UT to 10:35UT. In all panels, different colors represent different epochs. In (a–d) and (f–i), the solid lines are vertical profiles from the HIME-driven Global Ionosphere and Thermosphere Model (GITM) run, while the dotted lines are vertical profiles from Weimer-driven GITM run 2. In (e), the solid lines are the vertical profiles obtained by subtracting the solution of Weimer-driven GITM run 2 from the solution of the HIME-driven GITM run, and then divided by the solution from Weimer-driven GITM run 2.

back to approximately the same as it is at 10:30UT. The Joule heating from the HIME-driven run shown in Figure 8b exhibits similar profiles and temporal variation as the total power density from the HIME-driven run. In particular, the peak Joule heating enhancement around 120 km altitude at 10:31UT is similar to the peak total power density enhancement at the same altitude. Therefore, this is a short-lived heating event induced by the mesoscale electric field driving. In GITM, the Joule heating is calculated as (Thayer & Semeter, 2004; J. Zhu & Ridley, 2016):

$$\frac{dE}{dt} = \sum_i \frac{n_n m_n \nu_{ni}}{m_n + m_i} \left[3k_B (T_i - T_n) + m_i (\mathbf{u}_n - \mathbf{u}_i)^2\right] \quad (1)$$

where $n$ is the number density, $m$ is the mass, $T$ is the temperature, and $\mathbf{u}$ is the velocity, with the subscripts $n$ and $i$ represent neutrals and ions, respectively. $\nu_{ni}$ is the neutral-ion collision frequency, and $k_B$ is the Boltzmann coefficient. The term $3k_B(T_i - T_n)$ represents the ion-to-neutral heat transfer, while the term $m_i(\mathbf{u}_n - \mathbf{u}_i)^2$ represents the frictional heating. Given different definitions of frictional heating in the literature (Brekke & Kamide, 1996; Thayer & Semeter, 2004; J. Zhu & Ridley, 2016), here we adopt the frictional heating definition from Ozturk et al. (2020) and J. Zhu and Ridley (2016) for GITM modeling. To identify the direct source of the Joule heating enhancement in GITM modeling, we compute the percentage of the frictional heating out of the Joule heating from both Weimer-driven and HIME-driven runs, shown in Figure 8c. In Weimer-driven run 2 and at all altitudes between 100 and 200 km, the contribution from the frictional heating to the Joule heating remains approximately unchanged during 10:30UT–10:35UT. In the HIME-driven run, the contribution from the frictional heating to the Joule heating increases by 20% from 10:30UT to 10:31UT at around 120 km altitude. This indicates that the neutral and ion velocity difference plays a more important role than the neutral and ion temperature difference in enhancing the Joule heating. More specifically, the neutral and ion velocity may deviate more as the ion velocity immediately follows variations in the electric field. The deviation of the neutral and ion velocities causes enhanced frictional heating and thus enhanced Joule heating. This is the dominant mechanism for the mesoscale electric field variability to increase the Joule heating during the time interval. The result is in synergy with the modeling result obtained by Matsuo and Richmond (2008), that the electric field variability effectively influences the ion-drag forcing on the neutrals.

We consider the thermospheric state at 10:30UT as the initial state and focus on the simulated neutral response to the heating event in the HIME-driven run. Figure 8d shows the neutral temperature from 10:30UT to 10:35UT. At 10:30UT, the neutral temperature from the HIME-driven run is already higher than the neutral temperature from Weimer-driven run 2. In the HIME-driven run, the response of the neutral temperature to the heating event is immediate. The neutral temperature enhances and reaches its maximum at 10:31UT, which is maintained for another minute. The neutral temperature enhancement occurs for all altitudes, with the largest enhancement of about 20 K between 250 and 350 km. At 10:33UT, the neutral temperature above 200 km reduces toward its initial state at 10:30UT. After 10:33UT, the neutral temperature above 300 km altitude further reduces and becomes even less than its initial state above 300 km altitude. Shown in Figure 8e, the neutral density responds to the heating event starting at 10:31UT with increased neutral density above 250 km altitude. The neutral density continues to enhance over time, and reaches the maximum enhancement at 10:35UT. Though not shown, the neutral density reduces after 10:35UT. The maximum neutral density enhancement is about 40% of the neutral density from Weimer-driven run 2 at 500 km altitude. Figures 8g–8i displays the eastward, northward, and upward neutral wind from both the Weimer-driven and HIME-driven runs. The eastward neutral wind from the HIME-driven run is persistently larger than the eastward wind from Weimer-driven run 2 at all altitudes during 10:30UT–10:35UT. In the HIME-driven run, the eastward neutral wind between 120 and 250 km increases by about 20 m/s from 10:30UT to 10:31UT and starts to reduce after 10:31UT, while the eastward neutral wind above 300 km keeps increasing from 10:30UT to 10:35UT. The eastward neutral wind profile variation with time indicates that the eastward wind below 250 km responds to the heating event first and immediately, meanwhile the response of the eastward wind above 300 km builds over several minutes. The northward neutral wind from both Weimer-driven and HIME-driven runs are negative during the time interval, indicating a southward wind. The southward wind from the HIME-driven run enhances at altitudes above 130 km from 10:30UT to 10:33UT, and it remains approximately unchanged after 10:33UT. The vertical neutral wind from the HIME-driven run is larger than the vertical neutral wind from Weimer-driven run 2 above 200 km altitude at all time. The heating event causes mostly increase in the upward wind during 10:31UT–10:33UT, specifically, about 20 m/s increase between 300 and 360 km altitudes and more than 50 m/s increase at 500 km altitude. The total neutral wind speed including all

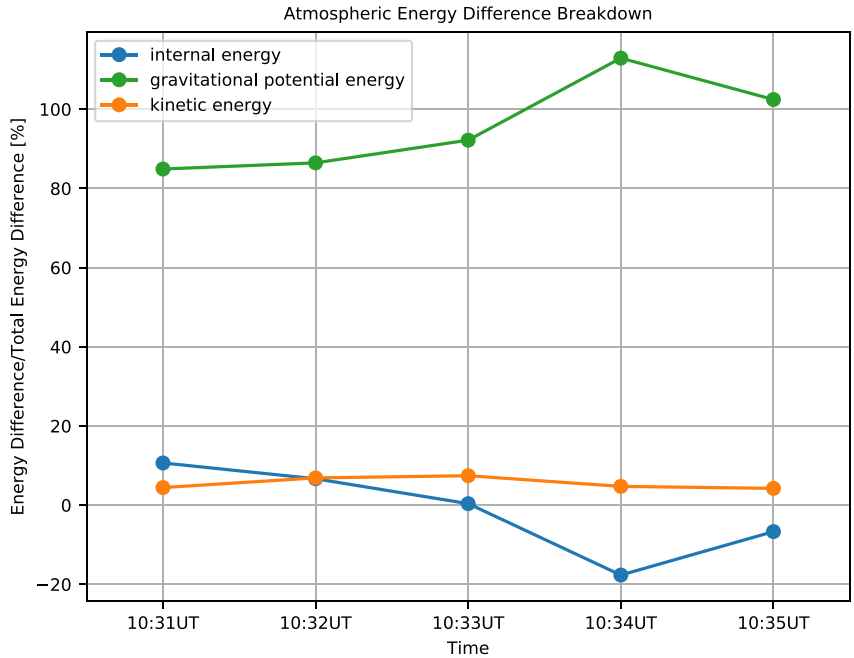


**Figure 9.** The decomposition of the atmospheric total energy change relative to its value at 10:30UT into internal energy, gravitational potential energy, and kinetic energy changes. The energies and the ratios are calculated according to Equations 2–5.

three directions is shown in Figure 8f. Unlike the nearly unchanged neutral wind speed from Weimer-driven run 2, the neutral wind speed from the HIME-driven run increases from 10:30UT to 10:33UT at almost all altitudes, and it reduces at 10:34UT. At 10:35UT, the neutral wind accelerates again, which is most likely due to the small heating enhancement from 10:34UT to 10:35UT. Hence, for the heating event at 10:31UT, the maximum response of the neutral wind speed occurs after 2 min, at 10:33UT, with the peak enhancement of about 30 m/s.

The above analysis indicates that the excess energy from the heating event deposits into the thermosphere via various pathways, that is, changing the neutral density and the neutral wind. To understand and quantify the energy deposition in the HIME-driven run, we calculate the atmospheric internal energy, gravitational potential energy, and kinetic energy, the three parts of the atmospheric energy, according to the following equations:

$$E_i = \int_{z=100km}^{500\text{km}} C_v \rho T_n \, dz \tag{2}$$

$$E_g = \int_{z=100km}^{500\text{km}} \rho g z \, dz \tag{3}$$

$$E_k = \int_{z=100km}^{500\text{km}} \frac{1}{2} \rho \mathbf{u_n}^2 \, dz \tag{4}$$

where $E_i$, $E_g$, $E_k$ are the internal energy, gravitational potential energy, and the kinetic energy, respectively. $C_v$ is the specific heat at constant volume, $\rho$ is the neutral density, and $z$ is the altitude. Values for $C_v$, $\rho$, $T_n$, and $\mathbf{u_n}$ are extracted from the HIME-driven GITM run at the single grid point 144.375°W and 67.125°N and vary with altitude. To compare temporal changes of the three types of energy, we calculate the following energy ratio every minute from 10:31UT to 10:35UT for all three types of energy:

$$Ratio_x = \frac{E_{x,t} - E_{x,10:30UT}}{E_{i,t} + E_{g,t} + E_{k,t} - E_{i,10:30UT} - E_{g,10:30UT} - E_{k,10:30UT}} \tag{5}$$

where subscript $x$ can be $i$, $g$, or $k$, and subscript $t$ can be 10:31$UT$, 10:32$UT$, 10:33$UT$, 10:34$UT$, or 10:35$UT$. Figure 9 displays the computed $Ratio_i$, $Ratio_g$, and $Ratio_k$ in percentage. During the time interval, the excess

heating goes mostly into the gravitational potential energy (more than 80%), while only a small portion becomes the kinetic energy. Interestingly, the internal energy ratio drops from 10:31UT to 10:34UT, indicating a reduced internal energy. This is compensated by the increase of the gravitational potential energy. Overall, the gravitational potential energy is the dominate energy pathway in the thermosphere during the heating event.

## 4. Conclusions

To understand the effects of mesoscale high-latitude electric fields on the thermosphere, we apply the HIME framework and its interface with GITM to conduct a case study of the thermospheric responses to mesoscale high-latitude electric field driving. For the first time we quantify the thermospheric energy budget driven by mesoscale electric fields and explored partitioning of excess heating. In the work, we focus on the high-latitude local region nearby PFISR during the recovery phase of a geomagnetic storm on 26 October 2019 when moderate substorm activities were present. The high-latitude electric field for driving GITM is specified via HIME by incorporating the electric field estimates based on PFISR measurements of the ion velocity during the time interval of interest. The adoption of the electric field estimates from PFISR measurements not only generates a stronger electric field compared to the electric field from empirical model Weimer, but also includes realistic mesoscale temporal and spatial variabilities of the electric field. Our modeling result indicates that the inclusion of the mesoscale variabilities in the electric field driving significantly alters the thermospheric energy budget primarily via enhanced Joule heating. The Joule heating enhancement in the local region of interest can reach up to five times of the Joule heating from the simulation driven by the empirical large-scale electric field of the same average magnitude as the mesoscale electric field. Meanwhile, the mesoscale electric field induces more temporal variations on time scales of minutes in the Joule heating. The simulated Joule heating from the HIME-driven GITM simulation that includes mesoscale electric field driving matches with observations much better than the Joule heating from the Weimer-driven GITM simulations. Considering all energy sources and sinks, the total power flux can increase by more than 100% and possesses more temporal variations in response to the mesoscale electric field driving. The enhancement in the total power flux goes immediately into the heating of the thermosphere. Quantitatively, a 1 $mW/m^2$ enhancement of the total power flux can induce 50 K neutral temperature increase above 200 km altitude immediately and 40% neutral density increase above 250 km altitude a few minutes later. The analysis of a representative localized heating event indicates that the mesoscale electric field driving enhances the Joule heating mostly via increased frictional heating due to ion-neutral velocity difference. The excess energy introduced by the mesoscale electric field driving deposits primarily through the gravitational potential energy within a few minutes, indicated by the neutral density enhancement, and second the kinetic energy, indicated by the neutral wind acceleration.

The case study reveals the importance of using a realistic high-latitude electric field with mesoscale variabilities to drive ionospheric and thermospheric models. In particular, the influence of the mesoscale variabilities on the thermospheric energy balance is critical. Our analysis of the localized heating event indicates that the mesoscale variabilities in the electric field can induce short-lived thermospheric heating and a rapid response of the thermospheric density and wind in the local region of interest. It remains unclear whether the thermospheric impact of the localized and short-lived heating events extends to a larger geographic region, or whether a collective occurring of short-lived heating events at different locations can have a global impact on the thermosphere. Further investigations combining modeling and observations are required to address these open questions. In addition, our case study does not take into account possible mesoscale variabilities in the auroral particle precipitation, which can correlate with the mesoscale variabilities in the electric field and simultaneously impacts the thermosphere. The inclusion of the mesoscale particle precipitation to HIME is ongoing work and will be reported in a future publication.

## Data Availability Statement

The PFISR experiment "GITM1. v01" used in this study can be found at https://data.amisr.com/database/61/experiment/20191026.002/1/. The OMNI data used to driven GITM simulations is obtained from https://spdf.gsfc.nasa.gov/pub/data/omni/. The FISM solar irradiance data is obtained via https://lasp.colorado.edu/lisird/. The HIME version 1.0 is available at https://github.com/dcsozturk/hime. The interface between HIME and GITM is part of GITM, which is available at https://github.com/GITMCode/GITM. The modeling data produced by the GITM simulations and used in the paper is available at https://doi.org/10.48577/jpl.GBK7WJ.

**Acknowledgments**
Portion of this research was sponsored by the NASA ROSES 2016 Heliophysics LWS Science (NRA NNH16ZDA001N) Program and carried out at the Jet Propulsion Laboratory, California Institute of Technology, under contract with NASA. This work is also supported by the Poker Flat Incoherent Scatter Radar which is a major facility funded by the National Science Foundation through cooperative agreement AGS-1840962 to SRI International. The authors gratefully acknowledge Prof. Aaron Ridley at the University of Michigan for making GITM source code available. The authors also acknowledge J. H. King, N. Papitashvili at AdnetSystems, NASA/GSFC, and CDAWeb for providing the OMNI data. The computing resources supporting this work were provided by the NASA High-End Computing (HEC) Program through the NASA Advanced Supercomputing (NAS) Division at Ames Research Center.

## References

Baker, J. B. H., Zhang, Y., Greenwald, R. A., Paxton, L. J., & Morrison, D. (2004). Height-integrated Joule and auroral particle heating in the night side high latitude thermosphere. *Geophysical Research Letters*, *31*(9), L09807. https://doi.org/10.1029/2004GL019535

Brekke, A., & Kamide, Y. (1996). On the relationship between Joule and frictional heating in the polar ionosphere. *Journal of Atmospheric and Solar-Terrestrial Physics*, *58*(1–4), 139–143. https://doi.org/10.1016/0021-9169(95)00025-9

Chamberlin, P. C., Woods, T. N., & Eparvier, F. G. (2008). Flare irradiance spectral model (FISM): Flare component algorithms and results. *Space Weather*, *6*(5), S05001. https://doi.org/10.1029/2007sw000372

Codrescu, M. V., Fuller-Rowell, T. J., & Foster, J. C. (1995). On the importance of E-field variability for joule heating in the high-latitude thermosphere. *Journal of Geophysical Research*, *22*(17), 2393–2396. https://doi.org/10.1029/95gl01909

Codrescu, M. V., Fuller-Rowell, T. J., Foster, J. C., Holt, J. M., & Cariglia, S. J. (2000). Electric field variability associated with the Millstone Hill electric field model. *Journal of Geophysical Research*, *105*(A3), 5265–5273. https://doi.org/10.1029/1999ja900463

Codrescu, M. V., Fuller-Rowell, T. J., Munteanu, V., Minter, C. F., & Millward, G. H. (2008). Validation of the coupled thermosphere ionosphere plasmasphere electrodynamics model: CTIPE-mass spectrometer incoherent scatter temperature comparison. *Space Weather*, *6*, S09005. https://doi.org/10.1029/2007SW000364

Cousins, E., & Shepherd, S. G. (2012). Statistical characteristics of small-scale spatial and temporal electric field variability in the high-latitude ionosphere. *Journal of Geophysical Research*, *117*(A3), A03317. https://doi.org/10.1029/2011JA017383

Crowley, G., & Hackert, C. L. (2001). Quantification of high latitude electric field variability. *Journal of Geophysical Research*, *128*(14), 2783–2786. https://doi.org/10.1029/2000GL012624

Deng, Y., Maute, A., Richmond, A. D., & Roble, R. G. (2008). Analysis of thermospheric response to magnetospheric inputs. *Journal of Geophysical Research*, *113*(A4), A04301. https://doi.org/10.1029/2007JA012840

Deng, Y., Maute, A., Richmond, A. D., & Roble, R. G. (2009). Impact of electric field variability on joule heating and thermospheric temperature and density. *Geophysical Research Letters*, *36*(8), L08105. https://doi.org/10.1029/2008GL036916

Drob, D. P., Emmert, J. T., Crowley, G., Picone, J. M., Shepherd, G. G., Skinner, W., et al. (2008). An empirical model of the Earth's horizontal wind fields: HWM07. *Journal of Geophysical Research*, *113*, A12304. https://doi.org/10.1029/2008JA013668

Evans, D. S., Maynard, N. C., Troim, J., Jacobsen, T., & Egeland, A. (1977). Auroral vector electric field and particle comparisons. II—Electrodynamics of an arc. *Journal of Geophysical Research*, *82*(16), 2235–2249. https://doi.org/10.1029/JA082i016p02235

Golovchanskaya, I. V. (2008). Assessment of joule heating for the observed distributions of high-latitude electric fields. *Geophysical Research Letters*, *35*, L16102. https://doi.org/10.1029/2008GL034413

Hedin, A. (1991). Extension of the MSIS thermosphere model into the middle and lower atmosphere. *Journal of Geophysical Research*, *96*(A2), 1159–1172. https://doi.org/10.1029/90JA02125

Heinselman, C. J., & Nicolls, M. J. (2008). Bayesian approach to electric field and E-region neutral wind estimation with the poker flat advanced modular incoherent scatter radar. *Radio Science*, *43*, RS5013. https://doi.org/10.1029/2007RS003805

Kaeppler, S. R., Knipp, D. J., Verkhoglyadova, O. P., Kilcommons, L. M., & Zhan, W. (2022). Chapter 5—Electromagnetic energy input and dissipation. In Y. Nishimura, O. P. Verkhoglyadova, Y. Deng, & S.-R. Zhang (Eds.), *Cross-scale coupling and energy transfer in the magnetosphere-ionosphere-thermosphere system* (pp. 301–355). Elsevier. https://doi.org/10.1016/B978-0-12-821366-7.00006-8

Lu, G., Richmond, A. D., Lühr, H., & Paxton, L. (2016). High-latitude energy input and its impact on the thermosphere. *Journal of Geophysical Research*, *121*(7), 7108–7124. https://doi.org/10.1002/2015JA022294

Lu, X., Wu, H., Nishimura, T., Kaeppler, S. R., Meriwether, J. W., Li, J., & Shi, X. (2021). The ionosphere-thermosphere responses to multi-scale high-latitude drivers during the 2015 St. Patrick's day storm. In *AGU Fall Meeting Abstracts* (Vol. *2021*).

Matsuo, T., & Richmond, A. D. (2008). Effects of high-latitude ionospheric electric field variability on global thermospheric joule heating and mechanical energy transfer rate. *Journal of Geophysical Research*, *113*(A7), A07309. https://doi.org/10.1029/2007JA012993

Matsuo, T., Richmond, A. D., & Hensel, K. (2003). High-latitude ionospheric electric field variability and electric potential derived from DE-2 plasma drift measurements: Dependence on IMF and dipole tilt. *Journal of Geophysical Research*, *108*(A1), 1005. https://doi.org/10.1029/2002JA009429

Millward, G. H., Moffett, R. J., Quegan, S., & Fuller-Rowell, T. J. (1996). A coupled thermosphere ionosphere plasmasphere model (CTIP). In R. W. Schunk (Ed.), *STEP handbook on ionospheric models* (pp. 239–279). Utah State University.

Millward, G. H., Müller-Wodrag, I. C. F., Aylward, A. D., Fuller-Rowell, T. J., Richmond, A. D., & Moffett, R. J. (2001). An investigation into the influence of tidal forcing on F region equatorial vertical ion drift using a global ionosphere-thermosphere model with coupled electrodynamics. *Journal of Geophysical Research*, *106*(A11), 24733–24744. https://doi.org/10.1029/2000JA000342

Newell, P. T., Sotirelis, T., & Wing, S. (2009). Diffuse, monoenergetic, and broadband aurora: The global precipitation budget. *Journal of Geophysical Research*, *114*(A9), A09207. https://doi.org/10.1029/2009JA014326

Nicolls, M. J., Cosgrove, R., & Bahcivan, H. (2014). Estimating the vector electric field using monostatic, multibeam incoherent scatter radar measurements. *Radio Science*, *49*(11), 1124–1139. https://doi.org/10.1002/2014RS005519

Ozturk, D. S., Meng, X., Verkhoglyadova, O. P., Varney, R., Reimer, A. S., & Semeter, J. L. (2020). A new framework to incorporate high-latitude input for mesoscale electrodynamics. *Journal of Geophysical Research*, *125*(1), e2019JA027562. https://doi.org/10.1029/2019JA027562

Papitashvili, N. E., & King, J. H. (2020). OMNI 1-min Data [Dataset]. NASA Space Physics Data Facility. https://doi.org/10.48322/45bb-8792

Richmond, A. D., Ridley, E. C., & Roble, R. G. (1992). A thermosphere/ionosphere general circulation model with coupled electrodynamics. *Geophysical Research Letters*, *19*(6), 369–604. https://doi.org/10.1029/92GL00401

Ridley, A. J., Deng, Y., & Tóth, G. (2006). The global ionosphere-thermosphere model. *Journal of Atmospheric and Solar-Terrestrial Physics*, *68*(8), 839–864. https://doi.org/10.1016/j.jastp.2006.01.008

Sheng, C., Deng, Y., Chen, Y.-J., Heelis, R. A., & Huang, Y. (2019). Effects of alignment between particle precipitation and ion convection patterns on joule heating. *Journal of Geophysical Research*, *124*(6), 4905–4915. https://doi.org/10.1029/2018JA026446

Thayer, J. P., & Semeter, J. (2004). The convergence of magnetospheric energy flux in the polar atmosphere. *Journal of Atmospheric and Solar-Terrestrial Physics*, *66*(10), 807–824. https://doi.org/10.1016/j.jastp.2004.01.035

Verkhoglyadova, O. P., Meng, X., Mannucci, A. J., Mlynczak, M. G., Hunt, L. A., & Lu, G. (2017). Ionosphere-thermosphere energy budgets for the ICME storms of March 2013 and 2015 estimated with GITM and observational proxies. *Space Weather*, *15*(9), 1102–1124. https://doi.org/10.1002/2017SW001650

Verkhoglyadova, O. P., Meng, X., Mannucci, A. J., Tsurutani, B. T., Hunt, L. A., Mlynczak, M. G., et al. (2016). Estimation of energy budget of ionosphere-thermosphere system during two CIR-HSS events: Observations and modeling. *Journal of Space Weather and Space Climate*, *6*, A20. https://doi.org/10.1051/swsc/2016013

Weimer, D. R. (2005). Improved ionospheric electrodynamic models and application to calculating Joule heating rates. *Journal of Geophysical Research*, *110*, A05306. https://doi.org/10.1029/2004JA010884

Wu, H., Lu, X., Lu, G., Chu, X., Wang, W., Yu, Z., et al. (2020). Importance of regional-scale auroral precipitation and electrical field variability to the storm-time thermospheric temperature enhancement and inversion layer (TTEIL) in the Antarctic E region. *Journal of Geophysical Research*, *125*(9), e2020JA028224. https://doi.org/10.1029/2020JA028224

Zhan, W., Kaeppler, S. R., Larsen, M. F., Reimer, A., & Varney, R. (2021). An investigation of auroral E region energy exchange using Poker Flat Incoherent Scatter Radar observations during fall equinox conditions. *Journal of Geophysical Research*, *126*(10), e2021JA029371. https://doi.org/10.1029/2021JA029371

Zhu, J., & Ridley, A. J. (2016). Investigating the performance of simplified neutral-ion collisional heating rate in a global IT model. *Journal of Geophysical Research*, *121*(1), 578–588. https://doi.org/10.1002/2015JA021637

Zhu, Q., Deng, Y., Richmond, A., & Maute, A. (2018). Small-scale and mesoscale variabilities in the electric field and particle precipitation and their impacts on Joule heating. *Journal of Geophysical Research*, *123*(11), 9862–9872. https://doi.org/10.1029/2018JA025771

Zhu, Q., Deng, Y., Richmond, A., McGranaghan, R. M., & Maute, A. (2019). Impacts of multiscale FACs on the ionosphere-thermosphere system: GITM simulation. *Journal of Geophysical Research*, *124*(5), 3532–3542. https://doi.org/10.1029/2018JA026082